Atmospheric
Chemistry
and Physics
Discussions

1 # Intra-regional transport of black carbon between the south edge of

2 # North China Plain and Central China during winter haze episodes

3 Huang Zheng[1, 2], Shaofei Kong[1], Fangqi Wu[1], Yi Cheng[1], Zhenzhen Niu[1], Shurui Zheng[1], Guowei Yang[1], Liquan Yao[2],

4 Qin Yan[1,2], Jian Wu[1,2], Mingming Zheng[2,3], Nan Chen[3], Ke Xu[3], Yingying Yan[1], Dantong Liu[4], Delong Zhao[5], Tianliang

5 Zhao[6], Yongqing Bai[7], Shuanglin Li[1], and Shihua Qi[2]

6 [1]Department of Atmospheric Science, School of Environmental Sciences, China University of Geosciences, Wuhan, 430074,

7 China

8 [2]Department of Environmental Science and Technology, School of Environmental Sciences, China University of Geosciences,

9 Wuhan, 430074, China

10 [3]Hubei Provincial Environmental Monitoring Centre, Wuhan, 430072, China

11 [4]School of Earth, Atmospheric & Environmental Sciences, University of Manchester, M139PL, UK

12 [5]Beijing Weather Modification Office, Beijing, 100089, China

13 [6]School of Atmospheric Physics, Nanjing University of Information Science and Technology, Nanjing, 210044, China

14 [7]Hubei Key Laboratory for Heavy Rain Monitoring and Warning Research, Institute of Heavy Rain, China Meteorological

15 Administration, Wuhan, 430205, China

16 *Correspondence to*: Shaofei Kong (kongshaofei@cug.edu.cn)

17 **Abstract.** Black carbon (BC), from the incomplete combustion sources (mainly fossil fuel, biofuel and open biomass burning),

18 is chemically inertness and optical absorbance in the atmosphere. It has significant impacts on global climate, regional air

19 quality, and human health. During the transportation, its physical-chemical characteristics, optical properties and sources

20 would change dramatically. To investigate the BC properties (i.e., mass concentration, sources and optical properties) during

21 the intra-regional transport between the south edge of North China Plain (SE-NCP) and Central China (CC), simultaneous

22 observations of BC at a megacity (Wuhan, WH) in CC, three borderline cities (Xiangyang, XY, Suixian, SX and Hong'an, HA,

23 distributing from the west to east) between SE-NCP and CC and a city (Luohe, LH) in SE-NCP were conducted during the

24 typical winter haze episodes. Using Aethalometer, the highest equivalent BC (eBC) mass concentrations and aerosol absorption

25 coefficients (σ_{abs}) were found in the city (LH) at SE-NCP, followed by the borderline cities (XY, SX and HA) and megacity

26 (WH). The levels, sources, optical properties (i.e., σ_{abs} and absorption Ångström exponent, AAE) and geographic origins of

27 eBC were different between clean and pollution episodes. Compared to clean days, the higher eBC levels (increased by

28 26.4−163%) and σ_{abs} (increased by 18.2−236%) were found during pollution episodes due to more combustion of fossil fuel

29 (contributing for 51.1−277%), supported by the decreased AAE (by 7.40−12.7%). Non-parametric wind regression (NWR)

Atmospheric
Chemistry
and Physics
Discussions

30 and concentration-weighted trajectory (CWT) results showed that the geographic origins of biomass burning (BC_{bb}) and fossil

31 fuel (BC_{ff}) combustion derived BC were different. Based on cluster analysis of trajectories, air parcels from south direction

32 dominated for border sites during clean days, with contributions of 46.0−58.2%, while trajectories from the northeast had

33 higher contributions (37.5−51.2%) during pollution episodes. At the SE-NCP site (LH), transboundary influences from south

34 direction (CC) exhibited more frequent impact (with the air parcels from this direction contributed 47.8% of all the parcels)

35 on the ambient eBC levels during pollution episodes. At WH, eBC was mainly from the northeast transport route during the

36 whole observation period. Two transportation cases showed that from upwind to downwind direction, the mass concentrations

37 of eBC, BC_{bb} and BC_{ff} all increased, while AAE decreased. This study highlighted that intra-regional prevention and control

38 for dominated sources of specific sites should be considered to improve the regional air quality.

39 **1 Introduction**

40 Black carbon (BC), a distinct type of carbonaceous material has attracted much attention mainly due to its climate effects over

41 past decades (Hansen et al., 2000; Jacobson, 2000; Bond et al., 2013). BC can strongly absorb but reflect less visible light and

42 the direct radiative forcing is estimated to be +0.88 W m^{-2} (Bond et al., 2013). It is composed of small carbon spherules and

43 has large specific surface areas, which allows it to absorb aerosol, and provide substrate for atmospheric chemical reactions

44 (Liu et al., 2018a). BC also has adverse human health effects (Jansen et al., 2005; Cao et al., 2012) due to its absorption of

45 carcinogenic pollutants. Additionally, recent studies showed that BC can strongly impact the ambient air quality. For instance,

46 in urban areas, BC can enhance the haze pollution by modifying the planetary layer height, which was unfavorable to the

47 vertical dispersion of air pollutants (Ding et al., 2016). This "dome effect" is more substantial in rural areas under the same

48 BC conditions (Wang et al., 2018a). BC particle, coated with more materials can markedly amplify absorption and direct

49 radioactive forcing, which would further worsen the air quality (Peng et al., 2016; Liu et al., 2017a; Zhang et al., 2018). As

50 the transportation key points, the properties of BC at rural and urban sites needed to be emphasized, which is always ignored

51 in former field campaigns.

52 BC is formed only in combustion processes of carbon-based materials such as biomass and fossil fuels. The broadly reported

53 BC sources can be grouped into stationary sources (i.e., industrial emission), area sources such as residential coal/wood

54 combustion, open burning and mobile sources including diesel engines, etc. (Chow et al., 2011; Bond et al., 2013). To identify

55 the BC sources, several methods including aethalometer model, diagnosis ratios and radioactive carbon isotope have been

56 developed (Sandradewi et al., 2008; Verma et al., 2010; Zotter et al., 2016). Chow et al., (2011) summarized the ratios of

57 element carbon to $PM_{2.5}$ (expressed as percentage, %) from various sources and these ratios have been used to qualitatively

58 describe the BC sources (Liu et al., 2018a). Radiocarbon method can give the quantified results of BC sources as the

59 abundances of $^{14}C/^{12}C$ in fossil fuel and modern carbon sources (i.e., biogenic sources) are different. Radiocarbon method

60 coupled with laevoglucose, a tracer of biomass burning have been adopted in BC source apportionment (Zhang et al., 2015a;

61 Liu et al., 2017b; Mouteva. et al., 2017; Salma et al., 2017). However, the technical limitations and the high cost for ^{14}C

Atmospheric
Chemistry
and Physics
Discussions

62   measurement block the application of radiocarbon method to BC source apportionment. The aethalometer model is an

63   alternative method, which can attribute the BC to fossil fuel combustion and biomass burning. The source apportionment can

64   be conducted using multi-wavelengths BC data (Sandradewi et al., 2008; Liu et al., 2018a) and the validity was proved by ^{14}C

65   method (Zotter et al., 2016). Compared to other methods, aethalometer model can provide high-time resolution variation of

66   BC source contributions (Kalogridis et al., 2017; Liu et al., 2018a), which help to understand the atmospheric behaviors of BC,

67   especial for the temporal variations.

68   Atmospheric lifetime of BC varied from a few days to weeks and therefore, BC undergoes regional and intercontinental

69   transport (Bond et al., 2013). During the transport, its mixing state, morphology and optical properties will change (China et

70   al., 2015). As a result, BC has been observed in remote areas such as the polar regions (Huang et al., 2010; Weller et al., 2013;

71   Qi et al., 2017; Xu et al., 2017) and Tibetan Plateau (Cong et al., 2013). For instance, Qi et al., (2017) found that Asian

72   anthropogenic activities contributed 35−45% and biomass burning emissions from Siberian contributed 46−64% to the sources

73   of BC in Arctic in April 2008 by GEOS-Chem modeling. Similarly, Xu et al. (2017) also used the global transport model to

74   conclude that the anthropogenic emissions from eastern and southern Asia contributed most to the Arctic BC column loading

75   with percentages being 56% and 37% for spring and annual, respectively. To study the regional transport of BC, backward

76   trajectories and concentration-weighted trajectory (CWT) were always employed (Huang et al., 2010; Wang et al., 2017a). The

77   ratio of BC/CO ratio was adopted to study the BC aging during the transport processes (Verma et al., 2010; Pan et al., 2011;

78   Guo et al., 2017). Previous studies mostly focused on the impact of BC transportation on its physical-chemical properties

79   during aging at a given site (e.g., a megacity or a remote background site). A recent study indicated that in the south Ontario,

80   higher BC loading in the summer was partly from the trans-boundary fossil fuel derived BC emissions in the US (Healy et al.,

81   2017). To our knowledge, the interaction of BC transportation among various sites for a specific region has been rarely reported,

82   which may limit the understanding of regional-joint control for air pollution.

83   After continuous efforts, especially in the last five years, the spatial distribution pattern of air pollution has changed obviously

84   in China, and the positive result is that the average annual $PM_{2.5}$ concentration in Pearl River Delta (PRD) has achieved the

85   national secondary standard level (http://www.zhb.gov.cn/hjzl/zghjzkgb/lnzghjzkgb/). Now the key regions suffering from

86   severe $PM_{2.5}$ pollution are North China Plain (NCP), Yangtze River Delta (YRD), Sichuan Basin (SB), Fen-Wei River Basin

87   and Central China (CC). From Lin et al. (2018), it could be found that the air pollution areas at the south edge of North China

88   Plain (SE-NCP) and Central China were combined together and there existed obvious transportation routes between SE-NCP

89   and CC. The spatial distribution of aerosol optical depth (AOD) across China also verified that high values existed in Central

90   China (Tao et al., 2017). As an important chemical composition of $PM_{2.5}$, BC account for 7.1−25.3% (Huang et al., 2014) of

91    $PM_{2.5}$ mass. Despite large scale observation of ambient BC has been conducted (Table S1−S2), the BC studies are mainly

92   reported in NCP (Zhao et al., 2013; Ji et al., 2018; Liu et al., 2018b; Wang et al., 2017a), YRD (Zhuang et al., 2014, 2015,

93   2017), PRD (Cheng et al., 2008; Wu et al., 2009; Wang et al., 2017b) and Tibetan Plateau (TP) (Zhu et al., 2017; Niu et al.,

94   2018; Wang et al., 2018b). No studies have concerned the BC transportation and interaction between these key regions. BC

95   emission inventory suggests that different source categories exists between NCP and CC (Wang et al., 2014b; Qiu et al., 2016),

Atmospheric
Chemistry
and Physics
Discussions

96   especially for the residential coal combustion (Qin and Xie, 2012). It should be emphasized that during the winter period, there

97   were central-heating activities in NCP, while no heating activities existed in Central China. It implied that the sources of BC

98   should be quite different. Therefore, the special geographic locations and terrain of Central China (Fig. 1) makes it complex

99   but provide an ideal opportunity to understand the BC levels, optical properties, sources and their variation during intra-

100   regional transportation between the two polluted regions. However, corresponding researches have not been reported.

101   Therefore, the aims of this study were to (1) study the differences of BC levels, sources, and optical properties under different

102   air pollution situation at this region; (2) quantify the regional transportation of BC at multiple observation sites in CC and SE-

103   NCP. To study the BC sources, the diagnosis ratios and aethalometer model were used. The backward trajectory based methods

104   were employed to quantify the potential regional transport contribution. This paper firstly reported the sources of BC in Central

105   China and gave the direct evidence of BC properties variation during the regional transportation between two key regions of

106   China, which is helpful to develop effective countermeasures for mitigating regional air pollution.

2 Methodology

2.1 Observation plan

109   For the sites selection, we refereed to the trajectory of air masses reached to Wuhan for January 2017 (Figure S1) and found

110   that the north and northwest direction were the main directions. For the north direction, the air masses originated at the SE-

111   NCP and Luohe is just on the north routes and close to the origination region as the Figure 1 shown. Meanwhile, the Central

112   China is not an isolated region. From Figure 1, there were two obvious connection channels for $PM_{2.5}$ between SE-NCP and

113   CC, which was decided by the mountain crossing the two regions. Therefore, to investigate the regional transport of air

114   pollutants and also answer whether the pollutants in CC can be transported to SE-NCP in winter, five sites including WH, three

115   borderline cities (Xiangyang, XY; Suixian, SX and Hong'an, HA, distributing from the west to east) between NCP and CC

116   and a city (Luohe, LH) in SE-NCP were selected as shown in Figure 1. The observation site at Wuhan locates in the Hubei

117   Environmental Monitoring Centre, which is an urban site with no industrial emission sources. LH and XY sites are located in

118   the suburban areas. HA and SX sites belong to rural areas. The observation instruments were placed near the local environment

119   monitor stations and therefore, the six routine-monitored air pollutants including $PM_{2.5}$, PM_{10}, NO_2, SO_2, CO and O_3 were

120   available. Black carbon measurement instruments including Magee Scientific-AE31, AE33 and AE51 were deployed (Table

121   1). The observation periods started from 8th January after a regional snowfall event and ended at 25th January 2018 before

122   another snowfall event coming. The observation duration at the five sites are summarized in Table 1.

2.2 Instrument description

124   AE31 continuously collects the ambient BC on the quartz tape and measures the light singles on sampled spot (I) and

125   reference spot (I_0) and the light attenuation (ATN) is defined as:

126 $$ATN = -100 ln(\frac{I}{I_0})$$ (1)

127 It assumes the relation between BC mass loading and the delta of ATN as a result of BC deposited on the tape is linear. The

128 BC mass concentration is calculated as following:

129 $$BC = \frac{d(ATN)}{MAC} \times \frac{A}{V}$$ (2)

130 where MAC is the mass specific attenuation cross section (m^2 g^{-1}); A is the area of sampled spot (1.67 cm^2); V is the volume

131 of the sampled air passing through the tape. The disadvantage of AE31 is the filter loading effect, which needs further

132 correction to compensate (Petit et al., 2015). The BC absorption coefficient (b_{abs}, Mm^{-1}) is calculated as:

133 $$b_{abs} = \frac{BC \times MAC}{C \times R(ATN)}$$ (3)

134 where C is the calibration factor (2.14 for quartz material tape); R (ATN) is a correction factor for shadowing effect and it is

135 empirically determined using the compensation parameter f (Weingartner et al., 2003):

136 $$R(ATN) = \left(\frac{1}{f} - 1\right) \frac{ln(ATN)-ln(10)}{ln(50)-ln(10)} + 1$$ (4)

137 To overcome the shortage of loading effect, AE33 (dual spot) was developed. It also simultaneously measures the ATN at

138 seven wavelengths. Different to AE31, AE33 measures BC on two parallel spots on the fibre tape (Teflon-coated) with different

139 flow rate:

140 $$BC_1 = BC \times (1 - k \cdot ATN_1)$$ (5)

141 $$BC_2 = BC \times (1 - k \cdot ATN_2)$$ (6)

142 The loading compensation k is calculated according the equation (5) and (6) and the BC mass concentration is further calculated

143 as following:

144 $$BC = \frac{A[d(ATN)/100]}{F_1(1-\varphi)MAC \cdot C(1-k \ ATN_1)dt}$$ (7)

145 For AE33, the area of sampled spot (A) is 0.785 cm^2 and enhancement parameter (C) is 1.57 for Teflon-coated fibre. The

146 absorption coefficient (σ_{abs}, Mm^{-1}) by AE33 is estimated as multiplying BC mass concentration by MAC. More details about

147 the BC concentration calculation, parameters (i.e., f and MAC for different wavelengths) and the differences between AE31

148 and AE33 can be found in previous study (Rajesh and Ramachandran, 2018). AE51 measures the absorbance (ATN) of the

149 loaded spot (3 mm diameter) and the reference portion of the Teflon-coated borosilicate glass fiber using a stabilized 880 nm

150 LED light source. The flow rate of AE51 was set as 100 mL min^{-1} and more information about AE51 can be found online

151 (https://aethlabs.com/microaeth/ae51/tech-specs).

152 **2.3 Data processing**

153 **2.3.1 BC source apportionment**

154 BC absorbs the solar spectrum efficiently with a weak dependence on wavelength and the absorption Ångström exponent

155 (AAE) is used to describe this spectral dependence of absorption (Zhu et al., 2017). The AAE value varies significantly from

Atmospheric
Chemistry
and Physics
Discussions

156   one source to another, i.e., the AAE values for fossil fuel combustion and biomass burning derived BC are 1.0 and 2.0,

157   respectively (Sandradewi et al., 2008). Therefore, a BC source apportionment method was established based on the AAE

158   (Sandradewi et al., 2008) and was verified by ^{14}C method (Zotter et al., 2016).

159   Black carbon source apportionment using aethalometer model is based on the assumption that the aerosol absorption coefficient

160   is from fossil fuel combustion derived BC (BC_{ff}) and biomass burning derived BC (BC_{bb}). Because the absorption coefficients

161   at different wavelengths are different and the absorption of BC_{ff} and BC_{bb} follow different spectral dependencies. The Ångström

162   exponents: α_{ff} and α_{bb} are used to describe the dependencies of fossil fuel and biomass burning, respectively. The following

163   equations are used in BC source apportionment (Sandradewi et al., 2008):

164    $$\frac{b_{abs}(470nm)_{ff}}{b_{abs}(950nm)_{ff}} = \left(\frac{470}{950}\right)^{-\alpha_{ff}} \tag{8}$$

165    $$\frac{b_{abs}(470nm)_{bb}}{b_{abs}(950nm)_{bb}} = \left(\frac{470}{950}\right)^{-\alpha_{bb}} \tag{9}$$

166    $$b_{abs}(470nm) = b_{abs}(470nm)_{ff} + b_{abs}(470nm)_{bb} \tag{10}$$

167    $$b_{abs}(950nm) = b_{abs}(950nm)_{ff} + b_{abs}(950nm)_{bb} \tag{11}$$

168    $$BB(\%) = \frac{b_{abs}(950nm)_{bb}}{b_{abs}(950nm)} \tag{12}$$

169   where b_{abs} (470 nm) and b_{abs} (950 nm) are the black carbon absorption coefficients at 470 and 950 nm wavelengths, respectively.

170   Due to the single channel (λ=880 nm) of AE51, BC source apportionment results were not available at SX and XY and were

171   only reported for HA, LH and WH.

2.3.2 Assessment of surface transport

173   Generally, the north wind dominated in winter in CC and air pollutants can be transported from upwind direction (north) to

174   downwind direction (south). In order to evaluate the effects of regional transport, the surface transport under specific wind

175   direction and speed per unit time was calculated according to the previous study (Wang et al., 2018b):

176    $$f = \frac{1}{n}\sum_{i=1}^{n} C_i \times WS_i \times cos\theta_i \tag{13}$$

177   where f stands for the surface flux intensity of BC (μg s^{-1} m^{-2}); n is the sum of observation hours; WS_i and C_i stand for the

178   hourly average of wind speeds (m s^{-1}) and BC mass concentrations (μg m^{-3}) in the ith observation duration, respectively; θ_i

179   represents the angle differences between hourly wind direction and the defined transport directions (i.e., northwest-southeast

180   for HA, SX and WH and north-south direction for LH and XY).

2.4 Potential geographic origins

182   The concentration-weighted trajectory (CWT) is always used to assess the regional transport of air pollutants (Kong et al.,

183   2018; Zheng et al., 2018). This method is based on backward trajectory analysis. Prior to CWT analyses, the backward

184   trajectory calculating was firstly conducted in each sampling site. The input wind datasets into HYSPLIT are downloaded from

185   the Nation Oceanic Atmospheric Administration (NOAA) (ftp://arlftp.arlhq.noaa.gov/pub/archives/gdas1/). For backward

Atmospheric
Chemistry
and Physics
Discussions

186   trajectory analysis, the air masses reaching at each observation site during the sampling period were calculated for 24 times

187   with 1-hour resolution each day (starting from 0:00 to 23:00) at 200 m AGL (Fig. S2). These trajectories were than clustered

188   according to their geographic origins (Fig. 1). For CWT analysis, a user-friendly tool Zefir written in Igor was used (Petit et

189   al., 2017a). The domain covered by trajectories was divided into thousands of cells with 0.2º × 0.2º. More description about

190   CWT can be found in text S1.

191   **2.5 Auxiliary dataset**

192   Hourly meteorological dataset including sea level pressure, temperature, relative humidity, wind speed, wind direction and

193   visibility were acquired form the China Meteorological Data Service Centre (CMDC) (http://data.cma.cn, last accessed:

194   2018/1/26). The every 3-hour boundary layer height (BLH) was acquired from the NOAA's READY Archived Meteorology

195   online calculating program (http://ready.arl.noaa.gov/READYamet.php, last accessed: 2018/4/8). Figure S3 shows the hourly

196   averaged meteorological parameters at the five sites. The meteorological conditions at the five sites followed the same variation

197   trends. However, significant differences ($p < 0.01$) of these parameters were found (Table S3). For instance, the average

198   pressure, temperature and relative humidity at WH were significant higher ($p < 0.01$) than those at LH. For BLH, the mean

199   values of the five sites showed insignificant differences. .

200   As mentioned in section 2.1, the five observation sites were located next to the local air quality monitoring stations and

201   therefore, six air pollutants (PM_{10}, $PM_{2.5}$, SO_2, NO_2, CO and O_3) were available and the data were downloaded from the China

202   Environmental Monitoring Centre (http://www.cnemc.cn, last accessed: 2018/4/10). Figure S4 shows the hourly average of

203   six air pollutants at the five sites during the observation periods. The major air pollutant was $PM_{2.5}$ during the entire research

204   campaign. According to the Ambient Air Quality Standards (GB3095-2012), the air quality can be classified into clean, light

205   polluted and heavily polluted when $PM_{2.5}$ mass concentrations are less than 75, between 75−250 and greater than 250 μg m^{-3},

206   respectively. Similar air quality classification was also reported elsewhere (Zheng et al., 2015; Zhang et al., 2018). Detailed

207   information about the daily air quality of each site is shown in Fig. S5.

208   **3 Results and discussion**

209   **3.1 General characteristics**

210   Time series and box plots of the eBC concentrations (measured at 880 nm) at the five sites are shown in Fig. 2. The highest

211   eBC concentrations were observed at LH (8.48 ± 4.83 μg m^{-3}), followed by XY (7.35 ± 3.45 μg m^{-3}), HA (5.54 ± 2.59 μg m^{-3}),

212   SX (4.47 ± 2.90 μg m^{-3}), and Wuhan (3.91 ± 1.86 μg m^{-3}). Despite the sampling periods, site types, inlet of aerosol and

213   instruments were different between different studies (Table S1), BC was generally higher in North China and lower BC levels

214   were found in remote areas and coastal areas. From BC emission inventory, North and Central China hold higher BC emission

215   intensity (Qin and Xie, 2012; Yang et al., 2017), i.e., emission rates in Hubei and Henan provinces were about 0.6−1.0 g C m^{-2}

216   yr^{-1}, which were higher than other regions (Yang et al., 2017). Simulation results also suggested that near-surface

217   concentrations of BC (6−8 μg m^{-3}) in Hubei and Henan were higher than those in south China (4−6 μg m^{-3}) during winter

218   (Yang et al., 2017). Compared to the results in other countries, BC levels in this study were higher than those in Finland

219   (Hyvärinen et al., 2011), France (Petit et al., 2017b), Ontario (Healy et al., 2017), and south Africa (Chiloane et al., 2017).

220   For the aerosol absorption properties measured at seven wavelengths by aethalometer, the characteristics (i.e., temporal

221   variation) are generally consistent with each other and the corresponding properties for wavelength at 520 nm is mostly

222   discussed (Zhuang et al., 2015, 2017; Wang et al., 2017b). Therefore, we only discussed the absorption properties at $\lambda = 520$

223   nm. Figure 3 shows the frequency distribution of absorption coefficients (σ_{abs}) at various sites. σ_{abs} measured at HA, LH, and

224   WH exhibited a single peak pattern. The average values of σ_{abs} measured at HA, LH and WH were 86.0, 132 and 60.6 Mm^{-1},

225   respectively. Similar to the spatial distribution of BC levels, higher σ_{abs} was found in North and Central China, while lower

226   values observed in coastal areas and Tibetan Plateau (Table S2).

227   Figure 3 also shows the average absorption spectra measured at seven wavelengths for different sites. The power law fit was

228   used to calculate the AAE (Zhu et al., 2017). The highest average AAE value was found at LH (1.40), followed by WH (1.34)

229   and HA (1.32). The results indicated that the AAE was different at urban, suburban and rural sites. Generally, the AAE from

230   coal combustion (2.11−3.18) (Sun et al., 2017) and biomass burning (1.85−2.0) (Petit et al., 2017b) were higher than that from

231   traffic sources (0.8−1.1) (Sandradewi et al., 2008; Olson et al., 2015). Therefore, AAE in different sites suggested the different

232   energy consumption structure and more coal or biomass were burned in North China (i.e., LH in this study).

3.2 Clean days *vs* pollution episodes

234   Figure. 4 shows the eBC concentrations under different air pollution situation. It clearly shows that the eBC concentrations

235   increased as the deterioration of air quality. For instance, at LH, the average eBC concentrations were 3.39 ± 2.06 μg m^{-3}, 8.31

236   ± 4.55 μg m^{-3} and 13.0 ± 4.59 μg m^{-3}, respectively when the air quality was clean, light polluted and heavy polluted. The

237   average values of eBC increased by 163%, 139%, 96.2%, 51.8% and 26.4% at SX, XY, LH, HA and WH, respectively from

238   clean to pollution. The enhancement of eBC along with the deterioration of air quality was also reported elsewhere (Wang et

239   al., 2014a; Liu et al., 2016, 2018b). At LH and HA, the enhancement eBC level from clean to pollution period was due to both

240   the elevated BC emissions from biomass burning (BC$_{bb}$) and fossil fuel combustion (BC$_{ff}$) (Fig. 4b and 4c). The BC$_{ff}$ accounted

241   for a higher contribution to eBC and the percentages of BC$_{bb}$ to eBC decreased during the haze episodes (Fig. 4d). At WH, the

242   concentration and percentage of BC$_{bb}$ both decreased from clean to pollution, which suggested that more BC$_{ff}$ was emitted

243   during haze episodes. This finding was different with previous study conducted in Beijing that the percentage of BC$_{bb}$ to eBC

244   increased from clean to pollution episodes (Liu et al., 2018b). The differences suggested that the control of fossil fuel

245   combustion (vehicle emissions) instead of coal or biomass burning should be taken priority during the haze episodes in WH.

246   While it should give priority to biomass and coal combustion control in North China to prevent air pollution.

247   Additionally, the aerosol optical properties (σ_{abs} and AAE) also exhibited different levels under different air pollution situation.

248   Similar to eBC levels, the σ_{abs} also elevated by 11.7−254% as the air quality switched from clean to pollution (Fig. 4e). There

249 are more secondary aerosols (i.e., sulfate, nitrate) during the pollution episodes (Huang et al., 2014), and the increased

250 secondary aerosols would be more adsorbed on the surface of BC. The absorption of BC therefore enhanced via the lens effects

251 of these coated materials (Jacobson, 2000; Moffet and Prather, 2009). On the contrary, the AAE showed higher values during

252 clean days compared to pollution episodes (Fig. 4f). The decreasing of AAE from clean to polluted days was also reported

253 elsewhere (Zhang et al., 2015b) and it can be partly attributed to the source variation. For instance, the AAE for biomass

254 burning is about 2.0 while the AAE for fossil fuel combustion is about 1.0 (Sandradewi et al., 2008). Higher AAE values

255 during clean days suggested that more BC was from biomass burning and lower AAE indicated the dominance of fossil fuel

256 combustion during the pollution period (Fig. 4c).

257 Figure 5 shows the diurnal variations of eBC under different air quality. At HA, LH and SX, after sunrise, an increasing and a

258 peak value at about 09:00 local time (LT) were observed. This variation was more obvious during pollution days due to the

259 higher eBC levels. The morning peak may be related with the combined effects of increased biomass burning and fossil fuel

260 combustion emissions (Fig. S6). Additionally, the low mixing layer height in the morning also favored the accumulation of

261 eBC. After sunrise, with the elevation of BLH, the eBC levels decreased and the minimum occurred at about 15:00 (LT). In

262 the evening hours, eBC showed increasing trends and peaks at about 21:00. The same diurnal patterns of eBC were also

263 reported in other areas (Verma et al., 2010; Ji et al., 2017; Liu et al., 2018b). However, the diurnal variations of eBC at WH

264 and XY exhibited different patterns during clean or pollution episodes. The diurnal pattern of eBC at WH was not likely

265 controlled by the development of mixing layer height, which may lead to the maximum and minimum values of air pollutants

266 generally occurring at sunrise and afternoon, respectively. The unexpected lower value in the morning (about 09:00 LT) and

267 higher value in the afternoon (15:00), at WH needs further research.

268 **3.3 Ratios of BC/PM$_{2.5}$ and BC/CO**

269 The BC/PM$_{2.5}$ and BC/CO ratios are widely used to identify the BC sources (Zhang et al., 2009; Wang et al., 2011; Verma et

270 al., 2010; Chow et al., 2011). Generally, the ratios of BC/PM$_{2.5}$ from oil combustion (traffic) and agricultural burning are higher

271 than those from industrial emissions such as manufacturing and mineral products. For instance, the mobile sources hold the

272 highest ratios of BC/PM$_{2.5}$ (0.33−0.77) and the residential wood combustion shows lower ratio (0.056) (Chow et al., 2011).

273 For the BC/CO ratios (μg m^{-3}/ppbv), it also varied from different sources, i.e., traffic (0.0052), industry (0.0072), power plant

274 (0.0177), and residential (0.0371) (Zhang et al., 2009). In this study, the BC, PM$_{2.5}$ and CO were well correlated with each

275 other (Fig. S7). The correlation coefficients (r^2) between BC and PM$_{2.5}$ were 0.67, 0.30, 0.44, 0.37 and 0.48 at LH, HA, WH,

276 SX and XY, respectively. Significant correlations ($p < 0.05$) between BC and CO were found with r^2 ranging from 0.27 (XY)

277 to 0.71 (LH). The good correlations indicated that the BC, PM$_{2.5}$ and CO may be from similar sources (except HA with low r

278 value as 0.06).

279 Overall, BC in this study was not likely from industrial emissions (Fig. 6a), as the BC/PM$_{2.5}$ ratios (μg m^{-3}/μg m^{-3}) in this

280 study (0.045−0.083) were higher than those from industry (0.0046−0.03) (Chow et al., 2011). Instead, BC/PM$_{2.5}$ ratios at the

281 five sites were all within the range of oil combustion (0.03−0.136). Additionally, the BC/PM$_{2.5}$ ratios at LH and SX were in

282   line with the ratio from residential wood combustion. From BC/CO ratios, BC was more likely from biomass burning (crop

283   residue: 0.0056−0.016) at HA and LH, while it was mainly from gasoline combustion in SX, WH, and XY (Fig. 6b). Quantified

284   calculation results using equations in section 2.3.1 also suggested that the fractions of BC from biomass burning at HA (27.6

285   ± 9.40%) and LH (29.5 ± 9.14%) were significant higher ($p < 0.01$) than that at WH (25.4 ± 11.8%). Compared to other urban

286   areas, the ratios of BC/CO (μg m^{-3}/ppbv) at SX (0.004), and WH (0.0044) were lower than those in Beijing (0.0058) (Han et

287   al., 2009), Guangzhou (0.0054) (Verma et al., 2010), Gwanjun (0.006) (Park, 2005) and Tokyo (0.0057) (Kondo et al., 2006)

288   as well as Mt. Huang (0.0065) (Pan et al., 2011), while ratios at HA (0.0091) and LH (0.0076) were higher than these studies.

289   Due to the longer atmospheric lifetime of CO, the ratio of BC to CO and the correlation coefficients of them would decreased

290   from upwind to downwind directions (Guo et al., 2017). Therefore, the BC/CO is used to reflect the BC aging during the

291   transport (McMeeking et al., 2010; Verma et al., 2010; Guo et al., 2017). Table 2 summarizes the BC/CO ratios at different

292   observation sites under different air pollution situation. Except for WH, clean days held significant lower BC/CO ratios than

293   those during the pollution episodes ($p < 0.01$). For instance, at LH, the BC/CO ratio during clean days (0.0058 ± 0.0024 μg

294   m^{-3}/ppbv) was significant lower ($p < 0.01$) than heavy pollution episodes (0.0071 ± 0.0013 μg m^{-3}/ppbv). The coefficients (r^2)

295   also decreased from pollution (0.52) to clean days (0.27). The BC/CO ratios suggested that when the air quality was good, BC

296   was more aged while it was fresher during the pollution episodes.

3.4 BC under different wind direction and speed

298   Nonparametric wind regression (NWR) was used to identify and quantify the impact of likely source regions of air pollutants

299   as defined by wind direction and speed (Henry et al., 2009). Fig. S8 shows the eBC levels under different wind speed and

300   directions at the five sites. As shown in Fig. 1, SX and HA are located in the northwest direction of WH and therefore, high

301   eBC levels were found in the northwest directions of SX, HA and WH when north wind dominated. On the contrary, when the

302   south wind dominated, BC was blowing from south to the north direction and high levels were found in the south direction at

303   WH and HA. However, at LH and XY, higher levels of BC were only found from south direction. In addition to eBC levels,

304   the BC$_{bb}$ and BC$_{ff}$ under different wind speed and directions were also discussed at HA, LH and WH (Fig. 7). At HA, the NWR

305   plots of BC$_{ff}$ was in line with eBC and high levels were from both northwest and south directions while the high level of BC$_{bb}$

306   was only found in southeast direction. The same result was also found at WH. High level of BC$_{bb}$ was due to more biomass

307   burning in the southeast direction of HA and WH. At LH, the NWR plots of BC$_{bb}$ and BC$_{ff}$ were the same with the eBC as

308   discussed above.

309   In order to describe the BC transportation from upwind to downwind directions, we used Eq. (6) in section 2.3.3 to calculate

310   the surface transport of eBC (Fig. 8). The calculated average SAT values of BC were −0.69 ± 10.2, −0.06 ± 12.0, −0.17 ± 5.33,

311   0.29 ± 6.14 and 0.99 ± 17.8 μg s^{-1} m^{-2}, respectively for HA, LH, SX, WH and XY. The negative values at HA, LH and SX

312   suggested that the transportation intensity of BC from south (southeast) to north (northwest) direction was higher, while the

313   positive values observed at WH and XY indicated that more BC was transported from north direction to south direction. The

314   large standard deviation of SAT reflected strong fluctuations in transport, which was due to wind speed, directions and BC

315   levels (Wang et al., 2018b).

3.5 Potential geographic origins

317   Employing CWT method, the potential geographic origins of eBC for the five sites were explored (Fig. S9). Overall, CWT

318   results of eBC at the five sites suggested that high eBC levels were found both in the north and south directions of LH and

319   WH, while the high levels (i.e., > 4 μg m^{-3}) of eBC were only found from northeast directions of HA, SX and XY (Fig. S9).

320   In addition to the possible geographic origins of eBC, the source regions of BC_{bb} and BC_{ff} at HA, LH and WH were also

321   discussed. At HA, the CWT results showed that high levels of eBC (i.e., > 3 μg m^{-3}) were from north /northeast direction.

322   However, the hot spots of BC_{bb} and BC_{ff} were different, with higher levels of BC_{bb} from both south and north directions and

323   higher levels of BC_{ff} from the north direction. The hot spots of BC_{bb} and BC_{ff} occurring in the north of HA were likely due to

324   the intensive BC emission in this area. Also, higher levels of BC_{bb} and BC_{ff} were found in the south of LH. Opposite to the

325   CWT results at HA, the hot spots of BC_{bb} was only found in the southeast direction of WH and high levels of BC_{ff} were found

326   in the north and south directions of WH. The CWT results at WH were in line with the wind rose plots in section 3.4. The unity

327   of CWT and wind rose plots at WH suggested that there were intensive biomass burning activities in the south direction of

328   WH during the observation period, which was verified by the MODIS fire-points distribution (Fig. S10).

329   Furthermore, we also discussed the source region differences of eBC under different air quality (Fig. 10). The higher levels

330   (>1 μg m^{-3}) of eBC were mainly from the south direction of HA when the air was clean. While during the pollution episodes,

331   air parcels from the north direction contributed high concentrations (> 3 μg m^{-3}) to the BC at HA. The CWT plots of BC_{bb} and

332   BC_{ff} showed similar distribution with eBC. At LH, CWT results of eBC, BC_{bb} and BC_{ff} showed that high levels of eBC were

333   mainly from south direction during clean days. When the air quality degraded to pollution, the air masses from south and east

334   directions both contributed to the high eBC (i.e., > 5 μg m^{-3} for BC) at LH. CWT results at WH showed that the southeast

335   direction was the dominant source regions of eBC, BC_{bb} and BC_{ff} during clean days, while the source regions switched to

336   northeast direction when the air quality changed into pollution.

337   To give quantified results of which cluster had greater contribution to eBC level at the receptor sites, the percentage

338   contributions of each cluster reaching at the five sites under different air pollution situation are summarized in Figure 11.

339   Trajectories from south was the main transport pathways reaching at HA, which accounted for 49.6% for clean days and

340   therefore, the highest average eBC level (6.33 ± 1.61 μg m^{-3}) was found from south direction during the clean days. However,

341   the percentage contribution for the south cluster contributed least (21.4%) to the total air masses, but it had the highest eBC

342   level (7.89 ± 2.59 μg m^{-3}) among the three clusters during the pollution episode. At LH, despite the lowest ratios of trajectories

343   were found from south (16.7%) and northwest (21.6%), respectively for clean and pollution days, these two clusters had the

344   highest eBC levels. At WH, the cluster with the highest percentages also had the highest BC levels. For instance, northeast

345   direction was the primary pathway of BC reaching at WH and the highest average eBC value was also found from this direction.

346   In summary, at the boundary sites (HA, SX and XY), BC was mainly from south direction (accounting for 46.0−58.2%) when

347   the air quality was clean and it was mainly from northeast/northwest directions (51.2−76.5%) when the air quality getting

348   worse. At SE-NCP site (LH), BC was dominantly from south direction (47.8%) during pollution episodes in this study. At CC

349   site (WH), BC was mainly from northeast direction (49.3−71.1%). These results suggested that northwest and northeast

350   directions were the main transport pathways of air pollutant reaching to WH during the pollution episodes. Furthermore, in

351   addition to control local emissions during haze episodes, the emission sources, i.e., industry plant and open biomass burning

352   in the upwind direction should also be controlled to prevent the further deterioration of air quality.

3.6 Case studies for BC properties variation during transportation

354   To explore the BC variations (i.e., mass concentration, sources and AAE) during the transportation, we chose two cases. LH

355   and HA were selected as the study sites due to the same instrument deployment (AE33) and they are representative of SE-NCP

356   and CC. BC transportation from HA to LH and from LH to HA were both considered. Figure 12a shows the hourly backward

357   trajectories reaching at HA on 2018-1-12 and the trajectory at 13:00 (UTC) was found passing through LH (black line) and the

358   travelling time was about 28 h. Therefore, the eBC mass concentration (including BC_{ff} and BC_{bb}) and AAE at the upwind site

359   LH on 8:00 2018-1-11 and downwind site HA on 13:00, 2018-1-13 (UTC) were compared. During the air transport from LH

360   to HA, eBC, BC_{ff} and BC_{bb} significantly increased ($p < 0.01$), while the AAE significantly decreased from 1.49 ± 0.02 to 1.42

361   ± 0.02 (p < 0.01). Similarly, in case 2, the air masses reaching at LH on 7:00, 2018-1-13 (UTC) were also passing through HA

362   before about 31 h ago (black line) (Figure 12c). The eBC and BC_{ff} increased from upwind (HA) to downwind (LH), while

363   BC_{bb} and AAE decreased from 2.37 ± 0.23 μg m^{-3} and 1.43 ± 0.02 to 12.14 ± 0.14 μg m^{-3} and 1.32 ± 0.01, respectively.

364   The eBC mass concentrations were found enhanced during the transportation regardless of the transport direction was from

365   CC to NCP or from NCP to CC. Previous studies found that the BC coagulation with non-refractory materials becomes more

366   significant when aging timescale greater than 10 h (Riemer et al., 2004). In these two cases, the travelling time (aging time)

367   from LH to HA and from HA to LH were 28 h and 31 h, respectively, which suggested that the BC particle should be coagulated

368   through complex atmospheric processes. Therefore, the new emission inputs along the trajectory enhanced the eBC mass

369   concentration during the transport. However, slight differences found for BC_{bb} transport: BC_{bb} increased from LH (1.28 ± 0.06

370   μg m^{-3}) to HA (2.57 ± 0.47 μg m^{-3}), while BC_{bb} decreased from HA (2.37 ± 0.23 μg m^{-3}) to LH (2.14 ± 0.14 μg m^{-3}). On the

371   contrary, the AAE values were found decreased during the transport. The same result was also found through numerical

372   simulation (Liu et al., 2018b). Additionally, chamber study of diesel soot particles coated with secondary organic compound

373   also found that the AAE decreased from 1.13 to 0.8 (Schnaiter, 2005). The decreasing of AAE of BC particles during the

374   transport indicated that BC was coated by other materials.

4 Summary

In order to understand the levels, optical properties, sources, regional transportation and aging of BC in Central China and south edge of North China Plain during winter haze episodes, simultaneous observations at rural sites (HA and SX), suburban (LH and XY) and megacity (WH) were conducted during January 2018. Using the diagnosis ratios, aethalometer model, backward trajectory and concentration-weighted trajectory (CWT) methods, conclusions were drawn as following:

(1) Generally, the highest ambient eBC was found in northern sites (8.48 ± 4.83 μg m^{-3} and 7.35 ± 3.45 μg m^{-3} at LH and XY), followed by the transport route sites (5.54 ± 2.59 μg m^{-3} and 4.47 ± 2.90 μg m^{-3} for and HA and SX), and southern site (3.91 ± 1.86 μg m^{-3} for WH).

(2) Levels, sources, optical properties, and diurnal variation of eBC were different under different air quality. eBC concentrations and absorption coefficients (σ_{abs}) increased by 26.4−163% and 11.7−254% respectively, from clean to pollution episodes. The increasing may due to more fossil fuel combustion emissions during pollution episodes, supported by lower Ångström exponent (AAE) and higher BC$_{ff}$ concentrations.

(3) BC/PM$_{2.5}$ and BC/CO ratios suggested that BC was mainly from oil combustion and residential wood or biomass combustion in this region. The higher BC/CO ratios during pollution episodes than those for clean days suggested that the BC particle was fresher during pollution days. (4) Nonparametric wind regression (NWR) results of BC$_{bb}$ and BC$_{ff}$ showed different dominate source regions with BC$_{bb}$ mainly from southeast direction and BC$_{ff}$ from both northwest and southeast of WH and HA. However, BC$_{bb}$ and BC$_{ff}$ were mainly from south direction of LH.

(5) At the boundary sites (HA, SX and XY), eBC was dominantly from south direction (accounting for 46.0−58.2%) when the air quality was clean and it was mainly from northeast/northwest directions (51.2−76.5%) during pollution episodes. At the SE-NCP site, air masses from south direction accounted for 47.8% of ambient BC level when the air was polluted. At the CC site, air parcels from northeast contributed 49.3−71.1% to the BC loading during the entire observation period (i.e., clean days and pollution episodes).

(6) During the transportation from upwind to downwind direction, BC mass concentration increased, while the AAE decreased. This study firstly revealed the differences of levels, optical properties and sources of BC at five sites in south edge of North China Plain and Central China during winter haze episodes and discussed the interaction of BC between two key polluted regions. It was expected to be a demonstration for corresponding researches on regional interaction of BC transportation during winter haze episodes for other regions.

Atmospheric
Chemistry
and Physics
Discussions

References

411 Andreae, M. O. and Merlet, P.: Emission of trace gases and aerosols from biomass burning, Glob. Biogeochem. Cycles, 15(4),
412   955–966, doi:10.1029/2000GB001382, 2001.

413 Bond, T. C., Doherty, S. J., Fahey, D. W., Forster, P. M., Berntsen, T., DeAngelo, B. J., Flanner, M. G., Ghan, S., Kärcher, B.,
414   Koch, D., Kinne, S., Kondo, Y., Quinn, P. K., Sarofim, M. C., Schultz, M. G., Schulz, M., Venkataraman, C., Zhang, H.,
415   Zhang, S., Bellouin, N., Guttikunda, S. K., Hopke, P. K., Jacobson, M. Z., Kaiser, J. W., Klimont, Z., Lohmann, U.,
416   Schwarz, J. P., Shindell, D., Storelvmo, T., Warren, S. G. and Zender, C. S.: Bounding the role of black carbon in the
417   climate system: A scientific assessment, J. Geophys. Res. Atmos., 118(11), 5380–5552, doi:10.1002/jgrd.50171, 2013.

418 Cao, G., Zhang, X., Gong, S. and Zheng, F.: Investigation on emission factors of particulate matter and gaseous pollutants
419   from crop residue burning, J. Environ. Sci., 20(1), 50–55, doi:10.1016/S1001-0742(08)60007-8, 2008.

420 Cao, J., Xu, H., Xu, Q., Chen, B. and Kan, H.: Fine particulate matter constituents and cardiopulmonary mortality in a heavily
421   polluted Chinese city, Environ. Health. Perspect., 120(3), 373–378, doi:10.1289/ehp.1103671, 2012.

422 Cheng, Y. F., Wiedensohler, A., Eichler, H., Su, H., Gnauk, T., Brüggemann, E., Herrmann, H., Heintzenberg, J., Slanina, J.
423   and Tuch, T.: Aerosol optical properties and related chemical apportionment at Xinken in Pearl River Delta of China,
424   Atmos. Environ., 42(25), 6351–6372, doi:10.1016/j.atmosenv.2008.02.034, 2008.

425 Chiloane, K. E., Beukes, J. P., van Zyl, P. G., Maritz, P., Vakkari, V., Josipovic, M., Venter, A. D., Jaars, K., Tiitta, P., Kulmala,
426   M., Wiedensohler, A., Liousse, C., Mkhatshwa, G. V., Ramandh, A. and Laakso, L.: Spatial, temporal and source
427   contribution assessments of black carbon over the northern interior of South Africa, Atmos. Chem. Phys., 17(10), 6177–
428   6196, doi:10.5194/acp-17-6177-2017, 2017.

429 China, S., Scarnato, B., Owen, R. C., Zhang, B., Ampadu, M. T., Kumar, S., Dzepina, K., Dziobak, M. P., Fialho, P., Perlinger,
430   J. A., Hueber, J., Helmig, D., Mazzoleni, L. R. and Mazzoleni, C.: Morphology and mixing state of aged soot particles at
431   a remote marine free troposphere site: implications for optical properties, Geophys. Res. Lett., 42(4), 1243–1250,
432   doi:10.1002/2014GL062404, 2015.

433 Chow, J. C., Watson, J. G., Lowenthal, D. H., Antony Chen, L. W. and Motallebi, N.: $PM_{2.5}$ source profiles for black and
434   organic carbon emission inventories, Atmos. Environ., 45(31), 5407–5414, doi:10.1016/j.atmosenv.2011.07.011, 2011.

435 Cong, Z., Kang, S., Gao, S., Zhang, Y., Li, Q. and Kawamura, K.: Historical trends of atmospheric black carbon on Tibetan
436   Plateau as reconstructed from a 150-year lake sediment record, Environ. Sci. Technol., 47(6), 2579–2586,
437   doi:10.1021/es3048202, 2013.

438   Dhammapala, R., Claiborn, C., Simpson, C. and Jimenez, J.: Emission factors from wheat and Kentucky bluegrass stubble
439   burning: comparison of field and simulated burn experiments, Atmos. Environ., 41(7), 1512–1520,
440   doi:10.1016/j.atmosenv.2006.10.008, 2007.

441   Ding, A. J., Huang, X., Nie, W., Sun, J. N., Kerminen, V. M., Petäjä, T., Su, H., Cheng, Y. F., Yang, X.-Q., Wang, M. H., Chi,
442   X. G., Wang, J. P., Virkkula, A., Guo, W. D., Yuan, J., Wang, S. Y., Zhang, R. J., Wu, Y. F., Song, Y., Zhu, T., Zilitinkevich,
443   S., Kulmala, M. and Fu, C. B.: Enhanced haze pollution by black carbon in megacities in China, Geophys. Res. Lett.,
444   43(6), 2873–2879, doi:10.1002/2016GL067745, 2016.

445   Guo, Q., Hu, M., Guo, S., Wu, Z., Peng, J. and Wu, Y.: The variability in the relationship between black carbon and carbon
446   monoxide over the eastern coast of China: BC aging during transport, Atmos. Chem. Phys., 17(17), 10395–10403,
447   doi:10.5194/acp-17-10395-2017, 2017.

448   Han, S., Kondo, Y., Oshima, N., Takegawa, N., Miyazaki, Y., Hu, M., Lin, P., Deng, Z., Zhao, Y., Sugimoto, N. and Wu, Y.:
449   Temporal variations of elemental carbon in Beijing, J. Geophys. Res., 114(D23), doi:10.1029/2009JD012027, 2009.

450   Hansen, J., Sato, M., Ruedy, R., Lacis, A. and Oinas, V.: Global warming in the twenty-first century: an alternative scenario,
451   Proc. Natl. Acad. Sci., 97(18), 9875–9880, doi:10.1073/pnas.170278997, 2000.

452   Healy, R. M., Sofowote, U., Su, Y., Debosz, J., Noble, M., Jeong, C. H., Wang, J. M., Hilker, N., Evans, G. J., Doerksen, G.,
453   Jones, K. and Munoz, A.: Ambient measurements and source apportionment of fossil fuel and biomass burning black
454   carbon in Ontario, Atmos. Environ., 161, 34–47, doi:10.1016/j.atmosenv.2017.04.034, 2017.

455   Henry, R., Norris, G. A., Vedantham, R. and Turner, J. R.: Source region identification using kernel smoothing, Environ. Sci.
456   Technol., 43(11), 4090–4097, doi:10.1021/es8011723, 2009.

457   Huang, L., Gong, S. L., Sharma, S., Lavoué, D. and Jia, C. Q.: A trajectory analysis of atmospheric transport of black carbon
458   aerosols to Canadian high Arctic in winter and spring (1990–2005), Atmos. Chem. Phys., 10(11), 5065–5073,
459   doi:10.5194/acp-10-5065-2010, 2010.

460   Huang, R. J., Zhang, Y., Bozzetti, C., Ho, K. F., Cao, J. J., Han, Y., Daellenbach, K. R., Slowik, J. G., Platt, S. M., Canonaco,
461   F., Zotter, P., Wolf, R., Pieber, S. M., Bruns, E. A., Crippa, M., Ciarelli, G., Piazzalunga, A., Schwikowski, M., Abbaszade,
462   G., Schnelle-Kreis, J., Zimmermann, R., An, Z., Szidat, S., Baltensperger, U., Haddad, I. E. and Prévôt, A. S. H.: High
463   secondary aerosol contribution to particulate pollution during haze events in China, Nature, 514(7521), 218–222,
464   doi:10.1038/nature13774, 2014.

465   Hyvärinen, A. P., Kolmonen, P., Kerminen, V. M., Virkkula, A., Leskinen, A., Komppula, M., Hatakka, J., Burkhart, J., Stohl,
466   A., Aalto, P., Kulmala, M., Lehtinen, K. E. J., Viisanen, Y. and Lihavainen, H.: Aerosol black carbon at five background
467   measurement sites over Finland, a gateway to the Arctic, Atmos. Environ., 45(24), 4042–4050,
468   doi:10.1016/j.atmosenv.2011.04.026, 2011.

469   Jacobson, M. Z.: A physically-based treatment of elemental carbon optics: implications for global direct forcing of aerosols,
470   Geophys. Res. Lett., 27(2), 217–220, doi:10.1029/1999GL010968, 2000.

471   Jansen, K. L., Larson, T. V., Koenig, J. Q., Mar, T. F., Fields, C., Stewart, J. and Lippmann, M.: Associations between health
472   effects and particulate matter and black carbon in subjects with respiratory disease, Environ. Health Perspect., 113(12),
473   1741–1746, doi:10.1289/ehp.8153, 2005.

474   Ji, D., Li, L., Pang, B., Xue, P., Wang, L., Wu, Y., Zhang, H. and Wang, Y.: Characterization of black carbon in an urban-rural
475   fringe area of Beijing, Environ. Pollut., 223, 524–534, doi:10.1016/j.envpol.2017.01.055, 2017.

476   Ji, D., Yan, Y., Wang, Z., He, J., Liu, B., Sun, Y., Gao, M., Li, Y., Cao, W., Cui, Y., Hu, B., Xin, J., Wang, L., Liu, Z., Tang, G.
477   and Wang, Y.: Two-year continuous measurements of carbonaceous aerosols in urban Beijing, China: temporal variations,
478   characteristics and source analyses, Chemosphere, 200, 191–200, doi:10.1016/j.chemosphere.2018.02.067, 2018.

479   Kalogridis, A. C., Vratolis, S., Liakakou, E., Gerasopoulos, E., Mihalopoulos, N. and Eleftheriadis, K.: Assessment of wood
480   burning versus fossil fuel contribution to wintertime black carbon and carbon monoxide concentrations in Athens, Greece,
481   Atmos. Chem. Phys. Discuss., 1–20, doi:10.5194/acp-2017-854, 2017.

482   Kondo, Y., Komazaki, Y., Miyazaki, Y., Moteki, N., Takegawa, N., Kodama, D., Deguchi, S., Nogami, M., Fukuda, M.,
483   Miyakawa, T., Morino, Y., Koike, M., Sakurai, H. and Ehara, K.: Temporal variations of elemental carbon in Tokyo, J.
484   Geophys. Res., 111(D12), doi:10.1029/2005JD006257, 2006.

485   Kong, S., Yan, Q., Zheng, H., Liu, H., Wang, W., Zheng, S., Yang, G., Zheng, M., Wu, J., Qi, S., Shen, G., Tang, L., Yin, Y.,
486   Zhao, T., Yu, H., Liu, D., Zhao, D., Zhang, T., Ruan, J. and Huang, M.: Substantial reductions in ambient PAHs pollution
487   and lives saved as a co-benefit of effective long-term $PM_{2.5}$ pollution controls, Environ. Int., 114, 266–279,
488   doi:10.1016/j.envint.2018.03.002, 2018.

489   Lin, C. Q., Liu, G., Lau, A. K. H., Li, Y., Li, C. C., Fung, J. C. H. and Lao, X. Q.: High-resolution satellite remote sensing of
490   provincial $PM_{2.5}$ trends in China from 2001 to 2015, Atmos. Environ., 180, 110–116, doi:10.1016/j.atmosenv.2018.02.045,
491   2018.

492   Liu, C., Chung, C. E., Yin, Y. and Schnaiter, M.: The absorption Ångström exponent of black carbon: from numerical aspects,
493   Atmos. Chem. Phys., 18(9), 6259–6273, doi:10.5194/acp-18-6259-2018, 2018a.

494   Liu, Y., Yan, C. and Zheng, M.: Source apportionment of black carbon during winter in Beijing, Sci. Total Environ., 618, 531–
495   541, doi:10.1016/j.scitotenv.2017.11.053, 2018b.

496   Liu, D., Whitehead, J., Alfarra, M. R., Reyes-Villegas, E., Spracklen, D. V., Reddington, C. L., Kong, S., Williams, P. I., Ting,
497   Y. C., Haslett, S., Taylor, J. W., Flynn, M. J., Morgan, W. T., McFiggans, G., Coe, H. and Allan, J. D.: Black-carbon
498   absorption enhancement in the atmosphere determined by particle mixing state, Nat. Geosci., 10(3), 184–188,
499   doi:10.1038/ngeo2901, 2017a.

500   Liu, D., Li, J., Cheng, Z., Zhong, G., Zhu, S., Ding, P., Shen, C., Tian, C., Chen, Y., Zhi, G. and Zhang, G.: Sources of non-
501   fossil-fuel emissions in carbonaceous aerosols during early winter in Chinese cities, Atmos. Chem. Phys., 17(18), 11491–
502   11502, doi:10.5194/acp-17-11491-2017, 2017b.

503   Liu, Q., Ma, T., Olson, M. R., Liu, Y., Zhang, T., Wu, Y. and Schauer, J. J.: Temporal variations of black carbon during haze
504   and non-haze days in Beijing, Sci. Rep., 6(1), doi:10.1038/srep33331, 2016.

505   McMeeking, G. R., Hamburger, T., Liu, D., Flynn, M., Morgan, W. T., Northway, M., Highwood, E. J., Krejci, R., Allan, J. D.,
506   Minikin, A. and Coe, H.: Black carbon measurements in the boundary layer over western and northern Europe, Atmos.
507   Chem. Phys., 10(19), 9393–9414, doi:10.5194/acp-10-9393-2010, 2010.

508   Moffet, R. C. and Prather, K. A.: In-situ measurements of the mixing state and optical properties of soot with implications for
509   radiative forcing estimates, Proc. Natl. Acad. Sci., 106(29), 11872–11877, doi:10.1073/pnas.0900040106, 2009.

510   Mouteva Gergana O., Randerson James T., Fahrni Simon M., Bush Susan E., Ehleringer James R., Xu Xiaomei, Santos
511   Guaciara M., Kuprov Roman, Schichtel Bret A. and Czimczik Claudia I.: Using radiocarbon to constrain black and
512   organic carbon aerosol sources in Salt Lake City, J. Geophys. Res. Atmos., 122(18), 9843–9857,
513   doi:10.1002/2017JD026519, 2017.

514   Niu, H., Kang, S., Wang, H., Zhang, R., Lu, X., Qian, Y., Paudyal, R., Wang, S., Shi, X. and Yan, X.: Seasonal variation and
515   light absorption property of carbonaceous aerosol in a typical glacier region of the southeastern Tibetan Plateau, Atmos.
516   Chem. Phys., 18(9), 6441–6460, doi:10.5194/acp-18-6441-2018, 2018.

517   Olson, M. R., Victoria Garcia, M., Robinson, M. A., Van Rooy, P., Dietenberger, M. A., Bergin, M. and Schauer, J. J.:
518   Investigation of black and brown carbon multiple-wavelength-dependent light absorption from biomass and fossil fuel
519   combustion source emissions, J. Geophys. Res. Atmos., 120(13), 6682–6697, doi:10.1002/2014JD022970, 2015.

520   Pan, X. L., Kanaya, Y., Wang, Z. F., Liu, Y., Pochanart, P., Akimoto, H., Sun, Y. L., Dong, H. B., Li, J., Irie, H. and Takigawa,
521   M.: Correlation of black carbon aerosol and carbon monoxide in the high-altitude environment of Mt. Huang in eastern
522   China, Atmos. Chem. Phys., 11(18), 9735–9747, doi:10.5194/acp-11-9735-2011, 2011.

523   Park, R. J.: Export efficiency of black carbon aerosol in continental outflow: global implications, J. Geophys. Res., 110(D11),
524   doi:10.1029/2004JD005432, 2005.

525   Peng, J., Hu, M., Guo, S., Du, Z., Zheng, J., Shang, D., Levy Zamora, M., Zeng, L., Shao, M., Wu, Y. S., Zheng, J., Wang, Y.,
526   Glen, C. R., Collins, D. R., Molina, M. J. and Zhang, R.: Markedly enhanced absorption and direct radiative forcing of
527   black carbon under polluted urban environments, Proc. Natl. Acad. Sci., 113(16), 4266–4271,
528   doi:10.1073/pnas.1602310113, 2016.

529   Petit, J. E., Favez, O., Sciare, J., Crenn, V., Sarda-Estève, R., Bonnaire, N., Močnik, G., Dupont, J. C., Haeffelin, M. and Leoz-
530   Garziandia, E.: Two years of near real-time chemical composition of submicron aerosols in the region of Paris using an
531   Aerosol Chemical Speciation Monitor (ACSM) and a multi-wavelength Aethalometer, Atmos. Chem. Phys., 15(6), 2985–
532   3005, doi:10.5194/acp-15-2985-2015, 2015.

533   Petit, J. E., Favez, O., Albinet, A. and Canonaco, F.: A user-friendly tool for comprehensive evaluation of the geographical
534   origins of atmospheric pollution: wind and trajectory analyses, Environ. Model. Softw., 88, 183–187,
535   doi:10.1016/j.envsoft.2016.11.022, 2017a.

536   Petit, J. E., Amodeo, T., Meleux, F., Bessagnet, B., Menut, L., Grenier, D., Pellan, Y., Ockler, A., Rocq, B., Gros, V., Sciare, J.
537   and Favez, O.: Characterising an intense PM pollution episode in March 2015 in France from multi-site approach and

538   near real time data: climatology, variabilities, geographical origins and model evaluation, Atmos. Environ., 155, 68–84,
539   doi:10.1016/j.atmosenv.2017.02.012, 2017b.

540 Qi, L., Li, Q., Henze, D. K., Tseng, H. L. and He, C.: Sources of springtime surface black carbon in the Arctic: an adjoint
541   analysis for April 2008, Atmos. Chem. Phys., 17(15), 9697–9716, doi:10.5194/acp-17-9697-2017, 2017.

542 Qin, Y. and Xie, S. D.: Spatial and temporal variation of anthropogenic black carbon emissions in China for the period 1980–
543   2009, Atmos. Chem. Phys., 12(11), 4825–4841, doi:10.5194/acp-12-4825-2012, 2012.

544 Qiu, X., Duan, L., Chai, F., Wang, S., Yu, Q. and Wang, S.: Deriving high-resolution emission inventory of open biomass
545   burning in China based on satellite observations, Environ. Sci. Technol., 50(21), 11779–11786,
546   doi:10.1021/acs.est.6b02705, 2016.

547 Rajesh, T. A. and Ramachandran, S.: Black carbon aerosol mass concentration, absorption and single scattering albedo from
548   single and dual spot aethalometers: radiative implications, J. Aerosol Sci., 119, 77–90, doi:10.1016/j.jaerosci.2018.02.001,
549   2018.

550 Riemer, N., Vogel, H. and Vogel, B.: Soot aging time scales in polluted regions during day and night, Atmos. Chem. Phys.,
551   4(7), 1885–1893, doi:10.5194/acp-4-1885-2004, 2004.

552 Salma, I., Németh, Z., Weidinger, T., Maenhaut, W., Claeys, M., Molnár, M., Major, I., Ajtai, T., Utry, N. and Bozóki, Z.:
553   Source apportionment of carbonaceous chemical species to fossil fuel combustion, biomass burning and biogenic
554   emissions by a coupled radiocarbon–levoglucosan marker method, Atmos. Chem. Phys., 17(22), 13767–13781,
555   doi:10.5194/acp-17-13767-2017, 2017.

556 Sandradewi, J., Prévôt, A. S. H., Szidat, S., Perron, N., Alfarra, M. R., Lanz, V. A., Weingartner, E. and Baltensperger, U.:
557   Using aerosol light absorption measurements for the quantitative determination of wood Burning and traffic emission
558   contributions to particulate matter, Environ. Sci. Technol., 42(9), 3316–3323, doi:10.1021/es702253m, 2008.

559 Schnaiter, M.: Absorption amplification of black carbon internally mixed with secondary organic aerosol, Journal of
560   Geophysical Research, 110(D19), doi:10.1029/2005JD006046, 2005.

561 Streets, D. G., Bond, T. C., Carmichael, G. R., Fernandes, S. D., Fu, Q., He, D., Klimont, Z., Nelson, S. M., Tsai, N. Y., Wang,
562   M. Q., Woo, J. H. and Yarber, K. F.: An inventory of gaseous and primary aerosol emissions in Asia in the year 200, J.
563   Geophys. Res. Atmos., 108(D21), doi:10.1029/2002JD003093, 2003.

564 Sun, J., Zhi, G., Hitzenberger, R., Chen, Y., Tian, C., Zhang, Y., Feng, Y., Cheng, M., Zhang, Y., Cai, J., Chen, F., Qiu, Y., Jiang,
565   Z., Li, J., Zhang, G. and Mo, Y.: Emission factors and light absorption properties of brown carbon from household coal
566   combustion in China, Atmos. Chem. Phys., 17(7), 4769–4780, doi:10.5194/acp-17-4769-2017, 2017.

567 Tao, J., Zhang, L., Cao, J. and Zhang, R.: A review of current knowledge concerning $PM_{2.5}$: chemical composition, aerosol
568   optical properties and their relationships across China, Atmos. Chem. Phys., 17(15), 9485–9518, doi:10.5194/acp-17-
569   9485-2017, 2017.

570   Verma, R. L., Sahu, L. K., Kondo, Y., Takegawa, N., Han, S., Jung, J. S., Kim, Y. J., Fan, S., Sugimoto, N., Shammaa, M. H.,
571   Zhang, Y. H. and Zhao, Y.: Temporal variations of black carbon in Guangzhou, China, in summer 2006, Atmos. Chem.
572   Phys., 10(14), 6471–6485, doi:10.5194/acp-10-6471-2010, 2010.

573   Wang, Y., Wang, X., Kondo, Y., Kajino, M., Munger, J. W. and Hao, J.: Black carbon and its correlation with trace gases at a
574   rural site in Beijing: top-down constraints from ambient measurements on bottom-up emissions, J. Geophys. Res. Atmos.,
575   116(D24), doi:10.1029/2011JD016575, 2011.

576   Wang, H., He, Q., Chen, Y. and Kang, Y.: Characterization of black carbon concentrations of haze with different intensities in
577   Shanghai by a three-year field measurement, Atmos. Environ., 99, 536–545, doi:10.1016/j.atmosenv.2014.10.025, 2014a.

578   Wang, R., Tao, S., Balkanski, Y., Ciais, P., Boucher, O., Liu, J., Piao, S., Shen, H., Vuolo, M. R., Valari, M., Chen, H., Chen,
579   Y., Cozic, A., Huang, Y., Li, B., Li, W., Shen, G., Wang, B. and Zhang, Y.: Exposure to ambient black carbon derived
580   from a unique inventory and high-resolution model, Proc. Natl. Acad. Sci., 111(7), 2459–2463,
581   doi:10.1073/pnas.1318763111, 2014b.

582   Wang, J., Virkkula, A., Gao, Y., Lee, S., Shen, Y., Chi, X., Nie, W., Liu, Q., Xu, Z., Huang, X., Wang, T., Cui, L. and Ding, A.:
583   Observations of aerosol optical properties at a coastal site in Hong Kong, South China, Atmos. Chem. Phys., 17(4), 2653–
584   2671, doi:10.5194/acp-17-2653-2017, 2017a.

585   Wang, Y., de Foy, B., Schauer, J. J., Olson, M. R., Zhang, Y., Li, Z. and Zhang, Y.: Impacts of regional transport on black
586   carbon in Huairou, Beijing, China, Environ. Pollut., 221, 75–84, doi:10.1016/j.envpol.2016.11.006, 2017b.

587   Wang, Q., Cao, J., Han, Y., Tian, J., Zhu, C., Zhang, Y., Zhang, N., Shen, Z., Ni, H., Zhao, S. and Wu, J.: Sources and
588   physicochemical characteristics of black carbon aerosol from the southeastern Tibetan Plateau: internal mixing enhances
589   light absorption, Atmos. Chem. Phys., 18(7), 4639–4656, doi:10.5194/acp-18-4639-2018, 2018a.

590   Wang, Z., Huang, X. and Ding, A.: Dome effect of black carbon and its key influencing factors: a one-dimensional modelling
591   study, Atmos. Chem. Phys., 18(4), 2821–2834, doi:10.5194/acp-18-2821-2018, 2018b.

592   Weingartner, E., Saathoff, H., Schnaiter, M., Streit, N., Bitnar, B. and Baltensperger, U.: Absorption of light by soot particles:
593   determination of the absorption coefficient by means of aethalometers, J. Aerosol Sci., 34(10), 1445–1463,
594   doi:10.1016/S0021-8502(03)00359-8, 2003.

595   Weller, R., Minikin, A., Petzold, A., Wagenbach, D. and König-Langlo, G.: Characterization of long-term and seasonal
596   variations of black carbon (BC) concentrations at Neumayer, Antarctica, Atmos. Chem. Phys, 13(3), 1579–1590,
597   doi:10.5194/acp-13-1579-2013, 2013.

598   Westerdahl, D., Wang, X., Pan, X. and Zhang, K. M.: Characterization of on-road vehicle emission factors and
599   microenvironmental air quality in Beijing, China, Atmos. Environ., 43(3), 697–705, doi:10.1016/j.atmosenv.2008.09.042,
600   2009.

601   Wu, D., Mao, J., Deng, X., Tie, X., Zhang, Y., Zeng, L., Li, F., Tan, H., Bi, X., Huang, X., Chen, J. and Deng, T.: Black carbon
602   aerosols and their radiative properties in the Pearl River Delta region, Sci. China Ser. Earth Sci., 52(8), 1152–1163,
603   doi:10.1007/s11430-009-0115-y, 2009.

Atmospheric
Chemistry
and Physics
Discussions

604   Xu, J. W., Martin, R. V., Morrow, A., Sharma, S., Huang, L., Leaitch, W. R., Burkart, J., Schulz, H., Zanatta, M., Willis, M. D.,
605   Henze, D. K., Lee, C. J., Herber, A. B. and Abbatt, J. P. D.: Source attribution of Arctic black carbon constrained by
606   aircraft and surface measurements, Atmos. Chem. Phys., 17(19), 11971–11989, doi:10.5194/acp-17-11971-2017, 2017.

607   Yang, Y., Wang, H., Smith, S. J., Ma, P. L. and Rasch, P. J.: Source attribution of black carbon and its direct radiative forcing
608   in China, Atmos. Chem. Phys., 17(6), 4319–4336, doi:10.5194/acp-17-4319-2017, 2017.

609   Zhang, Q., Streets, D. G., Carmichael, G. R., He, K. B., Huo, H., Kannari, A., Klimont, Z., Park, I. S., Reddy, S., Fu, J. S.,
610   Chen, D., Duan, L., Lei, Y., Wang, L. T. and Yao, Z. L.: Asian emissions in 2006 for the NASA INTEX-B mission, Atmos.
611   Chem. Phys., 9(14), 5131–5153, doi:10.5194/acp-9-5131-2009, 2009.

612   Zhang, X., Rao, R., Huang, Y., Mao, M., Berg, M. J. and Sun, W.: Black carbon aerosols in urban central China, J. Quant.
613   Spectrosc. Radiat. Transf., 150, 3–11, doi:10.1016/j.jqsrt.2014.03.006, 2015a.

614   Zhang, Y. L., Huang, R. J., El Haddad, I., Ho, K. F., Cao, J. J., Han, Y., Zotter, P., Bozzetti, C., Daellenbach, K. R., Canonaco,
615   F., Slowik, J. G., Salazar, G., Schwikowski, M., Schnelle-Kreis, J., Abbaszade, G., Zimmermann, R., Baltensperger, U.,
616   Prévôt, A. S. H. and Szidat, S.: Fossil vs. non-fossil sources of fine carbonaceous aerosols in four Chinese cities during
617   the extreme winter haze episode of 2013, Atmos. Chem. Phys., 15(3), 1299–1312, doi:10.5194/acp-15-1299-2015, 2015b.

618   Zhang, Y., Zhang, Q., Cheng, Y., Su, H., Li, H., Li, M., Zhang, X., Ding, A. and He, K.: Amplification of light absorption of
619   black carbon associated with air pollution, Atmos. Chem. Phys., 1–27, doi:10.5194/acp-2017-983, 2018.

620   Zhao, P., Dong, F., Yang, Y., He, D., Zhao, X., Zhang, W., Yao, Q. and Liu, H.: Characteristics of carbonaceous aerosol in the
621   region of Beijing, Tianjin, and Hebei, China, Atmos. Environ., 71, 389–398, doi:10.1016/j.atmosenv.2013.02.010, 2013.

622   Zheng, G. J., Duan, F. K., Su, H., Ma, Y. L., Cheng, Y., Zheng, B., Zhang, Q., Huang, T., Kimoto, T., Chang, D., Pöschl, U.,
623   Cheng, Y. F. and He, K. B.: Exploring the severe winter haze in Beijing: the impact of synoptic weather, regional transport
624   and heterogeneous reactions, Atmos. Chem. Phys., 15(6), 2969–2983, doi:10.5194/acp-15-2969-2015, 2015.

625   Zheng, H., Kong, S., Xing, X., Mao, Y., Hu, T., Ding, Y., Li, G., Liu, D., Li, S. and Qi, S.: Monitoring of volatile organic
626   compounds (VOCs) from an oil and gas station in northwest China for 1 year, Atmos. Chem. Phys., 18(7), 4567–4595,
627   doi:10.5194/acp-18-4567-2018, 2018.

628   Zhu, C. S., Cao, J. J., Hu, T. F., Shen, Z. X., Tie, X. X., Huang, H., Wang, Q. Y., Huang, R. J., Zhao, Z.Z., Močnik, G. and
629   Hansen, A. D. A.: Spectral dependence of aerosol light absorption at an urban and a remote site over the Tibetan Plateau,
630   Sci. Total Environ., 590–591, 14–21, doi:10.1016/j.scitotenv.2017.03.057, 2017.

631   Zhuang, B. L., Wang, T. J., Liu, J., Li, S., Xie, M., Yang, X. Q., Fu, C. B., Sun, J. N., Yin, C. Q., Liao, J. B., Zhu, J. L. and
632   Zhang, Y.: Continuous measurement of black carbon aerosol in urban Nanjing of Yangtze River Delta, China, Atmos.
633   Environ., 89, 415–424, doi:10.1016/j.atmosenv.2014.02.052, 2014.

634   Zhuang, B. L., Wang, T. J., Liu, J., Ma, Y., Yin, C. Q., Li, S., Xie, M., Han, Y., Zhu, J. L., Yang, X. Q. and Fu, C. B.: Absorption
635   coefficient of urban aerosol in Nanjing, west Yangtze River Delta, China, Atmos. Chem. Phys., 15(23), 13633–13646,
636   doi:10.5194/acp-15-13633-2015, 2015.

637 Zhuang, B., Wang, T., Liu, J., Li, S., Xie, M., Han, Y., Chen, P., Hu, Q., Yang, X., Fu, C. and Zhu, J.: The surface aerosol
638   optical properties in the urban area of Nanjing, west Yangtze River Delta, China, Atmos. Chem. Phys., 17(2), 1143–1160,
639   doi:10.5194/acp-17-1143-2017, 2017.
640 Zotter, P., Herich, H., Gysel, M., El-Haddad, I., Zhang, Y., Močnik, G., Hüglin, C., Baltensperger, U., Szidat, S. and Prévôt, A.
641   S. H.: Evaluation of the absorption Ångström exponents for traffic and wood burning in the Aethalometer based source
642   apportionment using radiocarbon measurements of ambient aerosol, Atmos. Chem. Phys. Discuss., 1–29,
643   doi:10.5194/acp-2016-621, 2016.
644

Atmospheric
Chemistry
and Physics
Discussions

Table 1 Information of the observation sites, periods and instruments

Sampling site	Location	Site type	Sampling period	Instrument	Data resolution
Hong'an (HA)	114.58º E, 31.24º N	Rural	1/8 13:00~1/25 9:00, 2018	AE33	1-minute
Luohe (LH)	114.05º E, 33.57º N	Suburban	1/9 18:00~1/25 9:00, 2018	AE33	1-minute
Suixian (SX)	113.28º E, 31.88º N	Rural	1/10 09:00~1/25 8:00, 2018	AE51	1-minute
Wuhan (WH)	114.39º E, 30.53º N	Urban	1/8 15:00~1/25 8:00, 2018	AE31	5-minute
Xiangyang (XY)	112.17º E, 32.02º N	Suburban	1/10 09:00~1/25 8:00, 2018	AE51	1-minute

Atmospheric
Chemistry
and Physics
Discussions

Table 2 Ratios of BC/CO (mean ± standard deviation) at the five sites under different air pollution situation

Sampling site	BC/CO (μg m^{-3}/ppbv)		
	Clean	Light pollution	Heavy pollution
HA	0.0048 ± 0.008	0.0057 ± 0.013	– [a]
LH	0.0058 ± 0.0024	0.0072 ± 0.0023	0.0071 ± 0.0013
SX	0.0025 ± 0.0013	0.0042 ± 0.0013	–
WH	0.0045 ± 0.0022	0.0042 ± 0.0017	–
XY	0.0048 ± 0.0020	0.0060 ± 0.0031	0.0071 ± 0.0040

[a] No heavy pollution episodes were observed
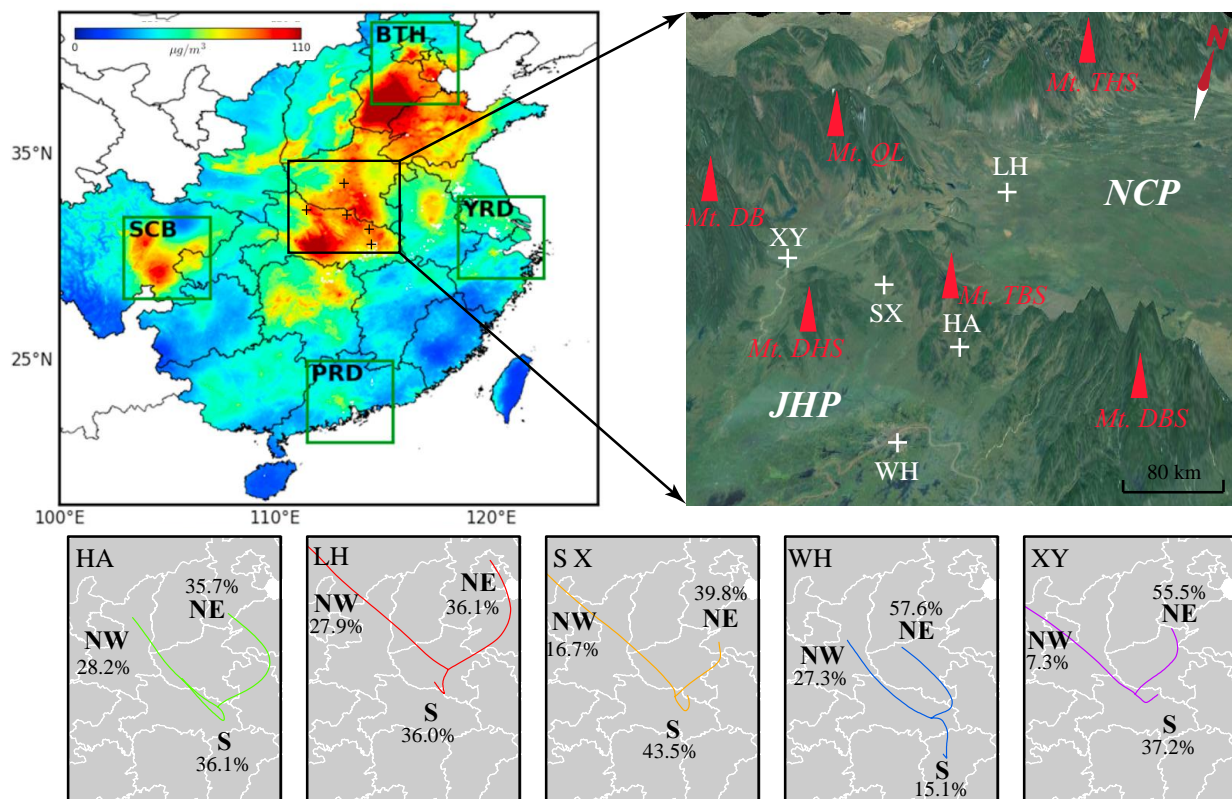
Figure 1 Location, terrain of the study area and clusters of backward trajectories reaching at each observation site. Up left is the spatial distribution of the 15 years average of PM$_{2.5}$ concentrations at a resolution of 1 km in the study region (Lin et al., 2018). Right up shows that the study area is surrounded by mountains and Mt. DBS and Mt. TBS blocks the North China Plain (NCP) and Jianghan Plian (JHP). Bottom shows that air masses reaching at the five sites were mainly from north directions (northwest and northeast) during the observation period.
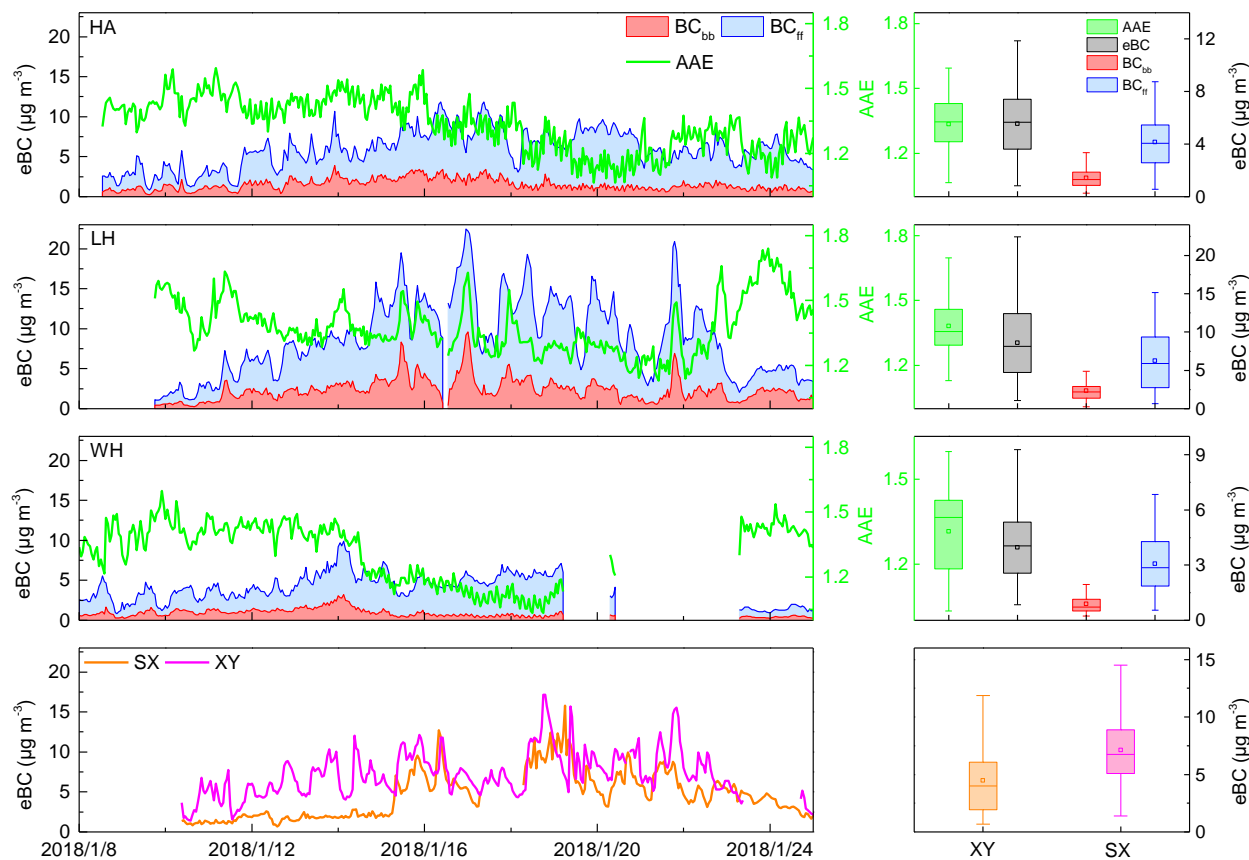
Figure 2 Time series and box plots of eBC, BC_{bb}, BC_{ff}, and absorption Ångström exponent (AAE) at the five sites during the observation period.

Atmospheric
Chemistry
and Physics
Discussions
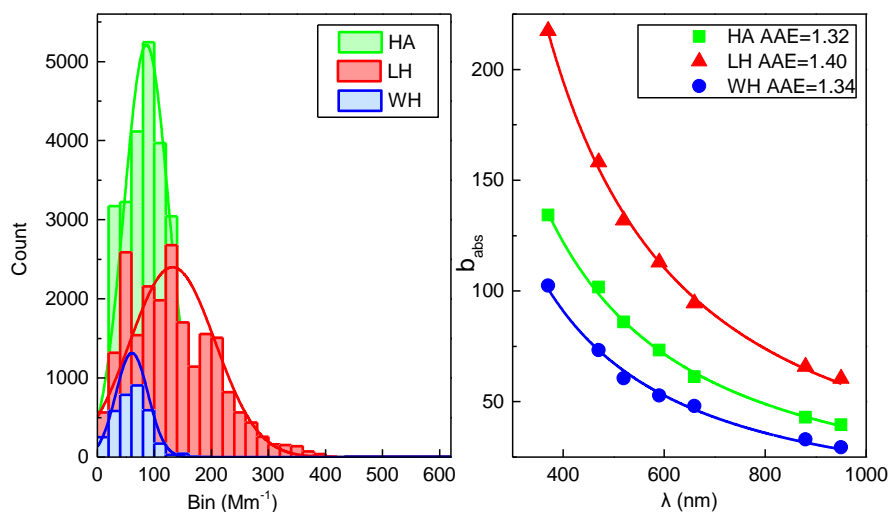
Figure 3 Frequency distribution of absorption coefficients (b_{abs}) at 520 nm wavelength (left panel) and power fit of b_{abs} at seven wavelengths (right panel) for HA, LH, and WH.
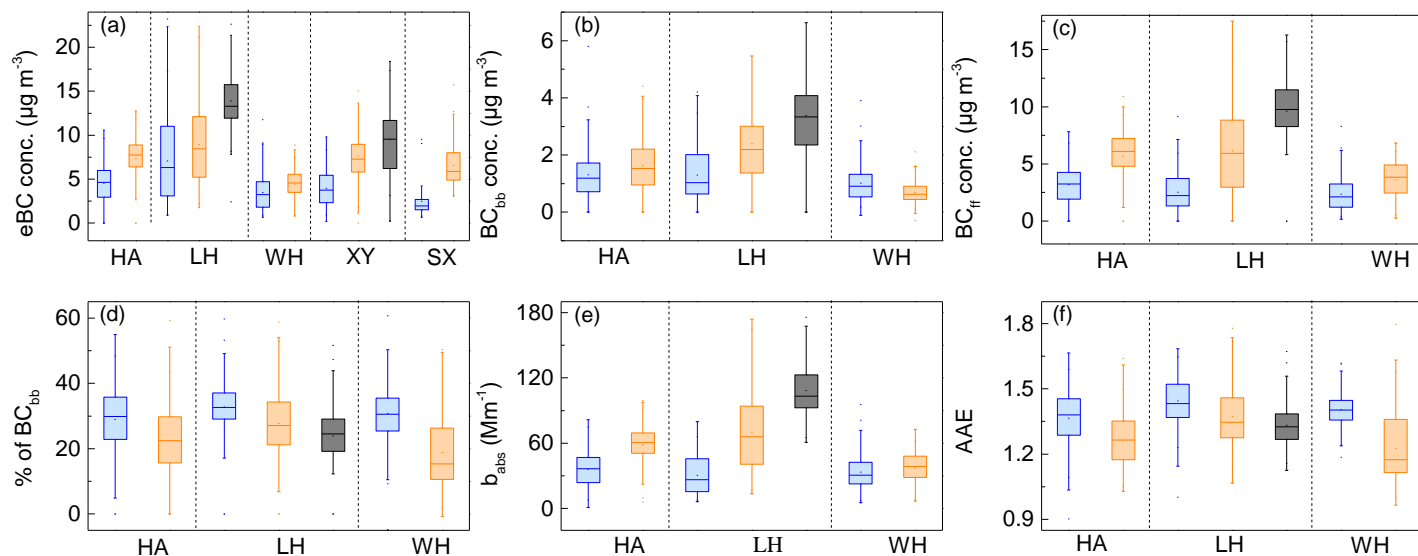
Figure 4 Box (25−75th percentiles) and whisker (5−95th percentiles) plots of eBC concentrations (a), BC_{bb} (b), BC_{ff} (c), percentages of BC_{bb} (d), aerosol absorption coefficients (e), and absorption Ångström exponent (AAE) under different air pollution situation. The blue, orange and black color represent the clean ($PM_{2.5} < 75$ μg m^{-3}), light pollution ($75 < PM_{2.5} < 250$ μg m^{-3}) and heavy pollution conditions ($PM_{2.5} > 250$ μg m^{-3}), respectively. The data number for the different air quality could be found in the supplementary file (Table S4).
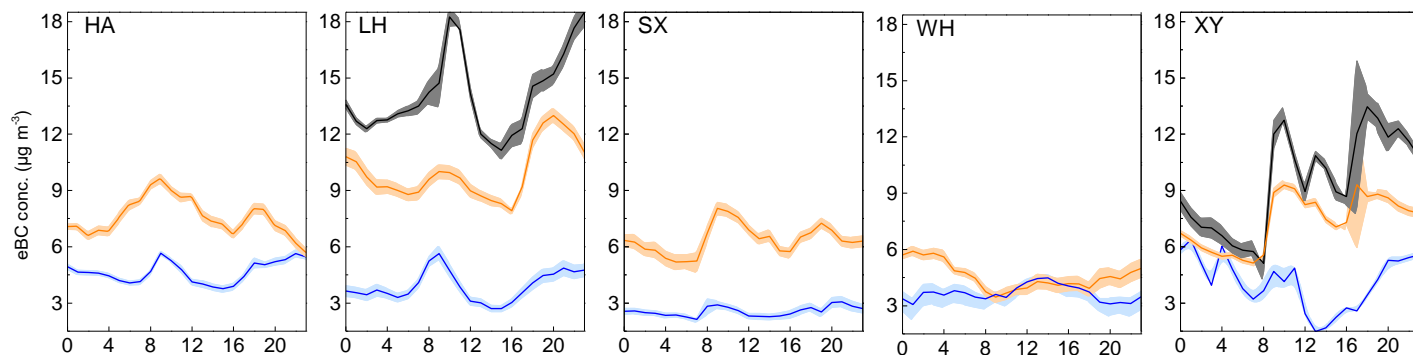
Figure 5 Diurnal variations of eBC under different air pollution situations (blue: clean; orange: light polluted; dark: heavy polluted) at the five observation sites. The solid lines are the average values and the filled ribbons are 95th confidential intervals of the average value.

28
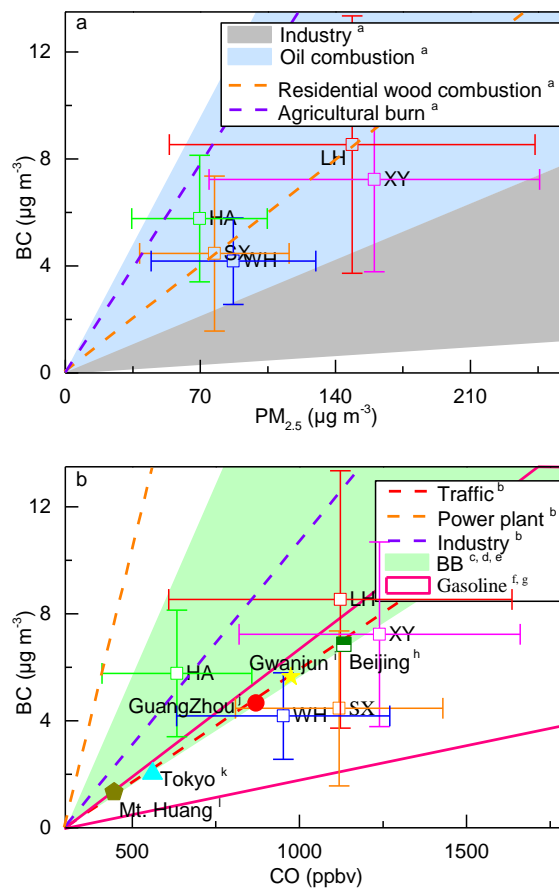
Figure 6 Ratios of BC/PM$_{2.5}$ (a) and BC/CO (b) in this study and previous researches.

[a] Chow et al., (2011); [b] Zhang et al., (2009); [c] Dhammapala et al., (2007); [d] Cao et al., (2008); [e] Andreae and Merlet, (2001); [f] Streets et al., (2003); [g] Westerdahl et al., (2009).
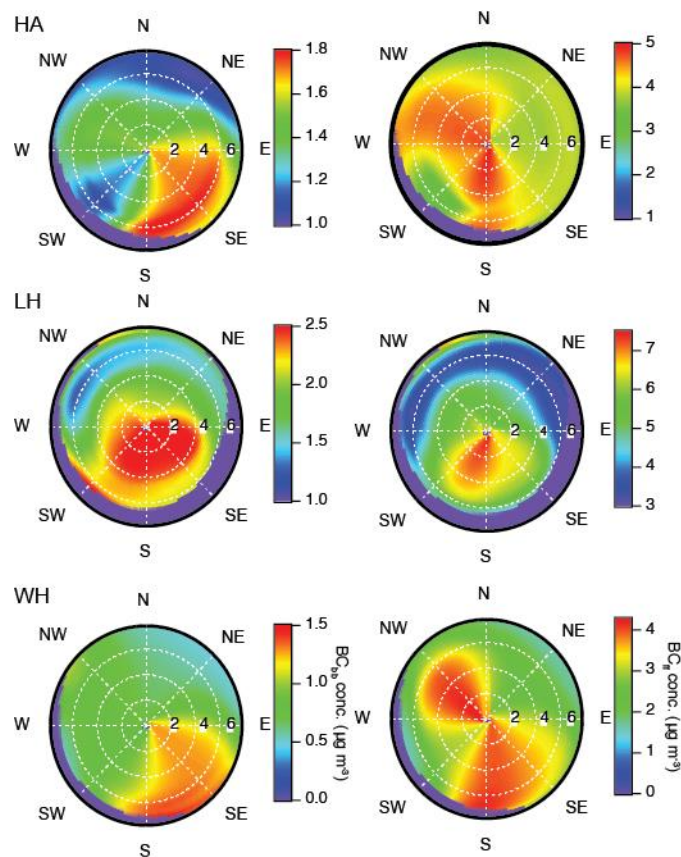
Figure 7 NWR plots of BC$_{bb}$ (left panel) and BC$_{ff}$ (right panel) at HA, LH and WH.
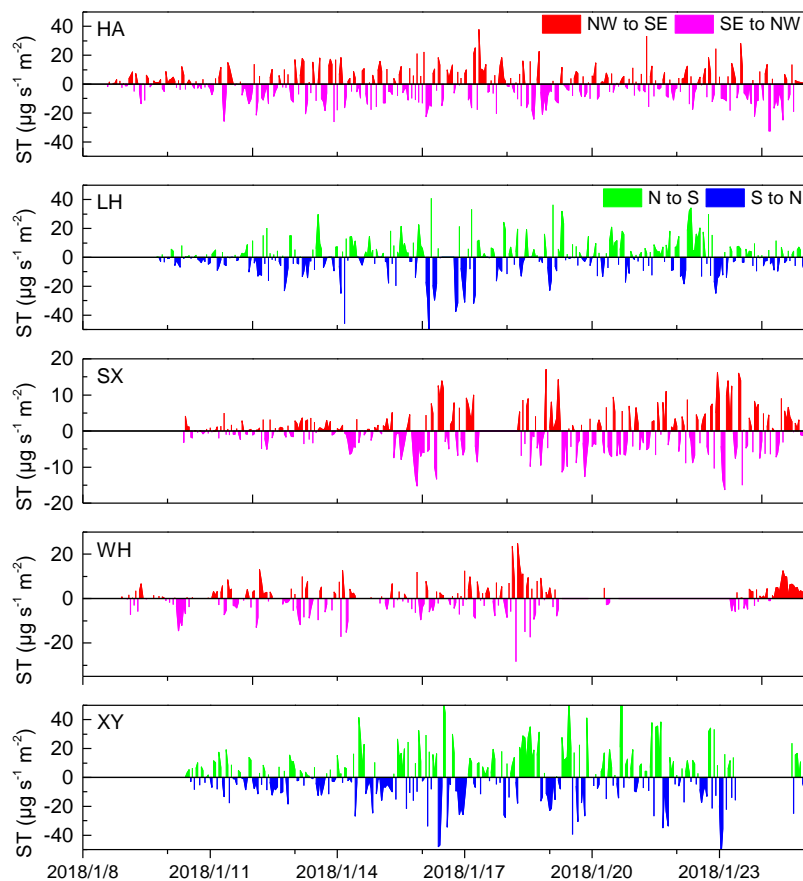
Figure 8 Time series of surface transport intensity for BC at the five observation sites. Positive values for HA and LH indicated the transport direction was from north to south and negative values indicated the transport direction was from south to north. Positive values for SX, WH and XY indicated the transport directions were from northwest to southeast and negative values indicated the transport directions were from southeast to northwest.
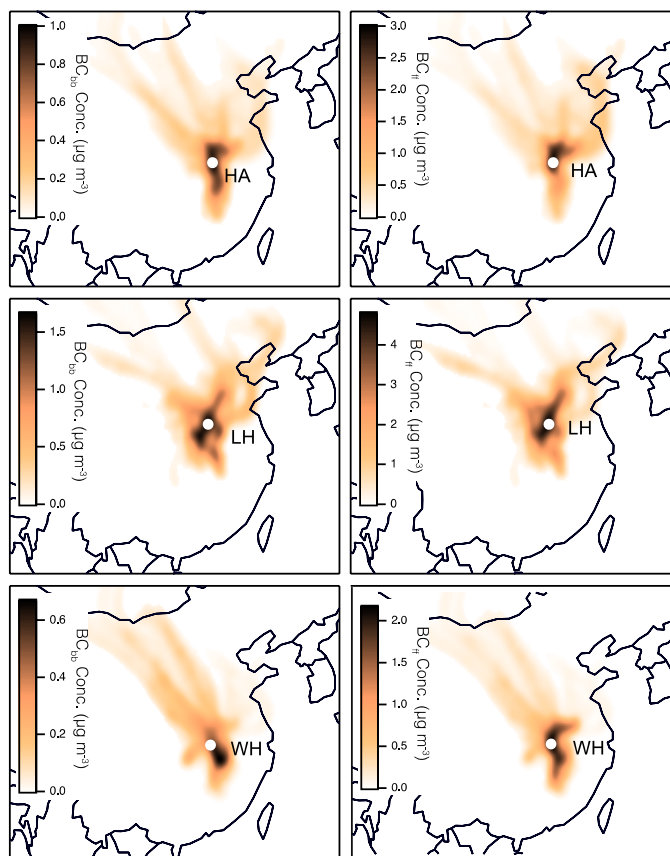
Figure 9 Concentration-weighted trajectory (CWT) plots of BC_{bb} (left panel) and BC_{ff} (right panel) at HA, LH and WH during the whole observation site. The white dote represents the observation site.

Figure 10 Concentration-weighted trajectory (CWT) plots of eBC, BC_{bb} and BC_{ff} during clean and pollution episodes at HA, LH and WH. The white dot represents the observation site.
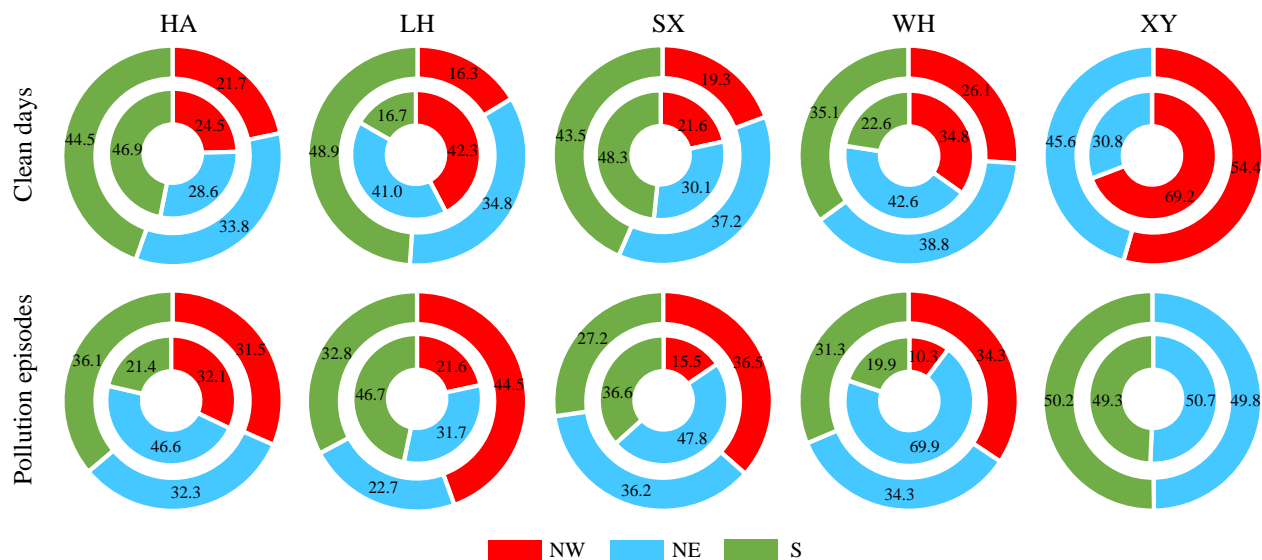
Figure 11 Cluster results at five sites (inner pie plots) and the eBC percentage contributions from different clusters (extern pie plot) during the clean days (up panel) and pollution episodes (bottom panel). NW, NE and S mean the northwest, northeast and south direction clusters as shown in Figure 1.
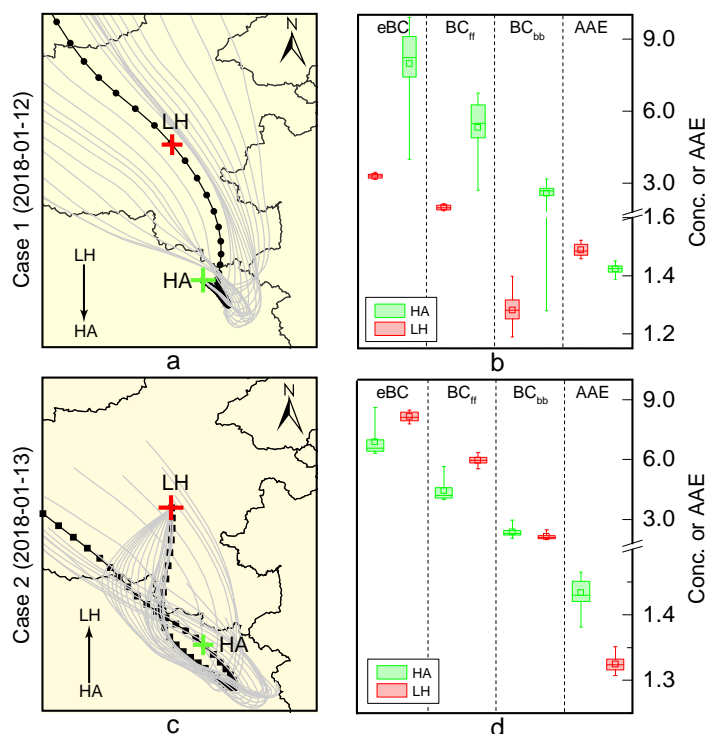
Figure 12 Case study of BC variation during the transportation from upwind to downwind direction. a (case 1): Hourly backward trajectories (grey line) reaching at HA on 2018-1-12 and the trajectory at 13:00 (UTC) (black line) was found passing through LH about 28 hours ago. c (case 2): Trajectory reaching at LH on 2018-1-13 07:00 (UCT) (black line) was found passing through HA about 31 hours ago. Box (25-75th percentiles) and whisker (5-95th percentiles) plots of eBC, BC_{ff}, BC_{bb} and AAE variation during the transport from LH to HA (b) and from HA to LH (d).